Supporting information for: Charge Distribution and Fermi Level in Bimetallic Nanoparticles

Nico Holmberg,[†] Kari Laasonen,[*,†] and Pekka Peljo[*,‡]

†*COMP Centre of Excellence in Computational Nanoscience, Department of Chemistry, Aalto University, P.O. Box 16100, FI-00076 Aalto, Finland*

‡*Laboratoire d'Electrochimie Physique et Analytique, École Polytechnique Fédérale de Lausanne, EPFL Valais Wallis, Rue de l'Industrie 17, Case Postale 440, CH-1951 Sion, Switzerland*

E-mail: kari.laasonen@aalto.fi; pekka.peljo@epfl.ch

1 Theory of Contact Electrification

Once two metals are brought into contact, electric charge flows from the metal with lower work function into the other until equilibrium is reached and the electrochemical potential of electrons in phases I and II have become equal.[S1]

$$\widetilde{\mu}_{e^-}^{\mathrm{I}} = \widetilde{\mu}_{e^-}^{\mathrm{II}} \tag{S1}$$

The electrochemical potential can be divided into real potential α (consisting of the chemical potential of electrons in the metal, i.e. the energy of electrons in a metal, and the work done to bring an electron into a neutral metal against its surface potential) and outer potential ψ contributions:

$$\alpha^{\mathrm{I}}_{e^-} - e\psi^{\mathrm{I}} = \alpha^{\mathrm{II}}_{e^-} - e\psi^{\mathrm{II}} \tag{S2}$$

Considering that the real potential of an electron in a metal is negative of the work function (real potential is the energy required to transport an electron from a state at rest in vacuum near the surface to a state inside the metal, while the work function is the energy of removal), the outer potential or the Volta potential difference is directly proportional to the difference in work functions:

$$\psi^{\mathrm{II}} - \psi^{\mathrm{I}} = \frac{\alpha^{\mathrm{II}}_{e^-} - \alpha^{\mathrm{I}}_{e^-}}{e} = \frac{\Phi^{\mathrm{I}} - \Phi^{\mathrm{II}}}{e} \tag{S3}$$

As the real chemical potential of electrons in a metal is an intrinsic property of this metallic phase, the equilibration of the Fermi level can only affect the outer potentials of the charged phases. Hence, the commonly used expression that "the vacuum level changes" upon contact electrification simply means that some of the charge transferred during the equilibration is distributed on the surfaces, resulting in an electric field, although most of the charge is retained at the metal contact interface as a surface dipole.

2 Electronic Structure Calculations

The reported electronic structure calculations have been performed with self-consistent DFT at the PBE/GGA[S2] level of theory. For nanoparticles, the spin-dependent Gaussian and plane waves method was used, as implemented in the freely-available CP2K/Quickstep computational code.[S3,S4] The $5d^{10}6s^1$ electrons of Au and the $4d^{10}5s^1$ electrons of Ag were treated as valence states. The valence orbitals were expanded in terms of molecularly optimized Gaussian basis sets of double-ζ plus polarization quality (MOLOPT-SR-DZVP).[S5] Core electrons were represented by norm-conserving Goedecker-Teter-Hutter pseudopotentials.[S6–S8] A 700 Ry kinetic energy cutoff was employed to truncate the auxiliary plane wave basis.

All nanoparticles were placed in vacuum inside a cubic simulation cell with 6 nm edge length. Interactions between periodic copies of the system were removed in each direction using the method of Martyna and Tuckerman.[S9] Atomic charges were determined by the Bader charge analysis method,[S10] which divides the real-space electron density into atom centered cells by computing the zero-flux surfaces of electron density between each atom pair. Net atomic charges were obtained by subtracting the core charge from the Bader charge.

For surface slab calculations, the GPAW[S11] implementation of the projector augmented wave (PAW) method was utilized. Again, 11 valence electrons were used to represent both Ag and Au. K-points in the 1st Brillouin zone were sampled using either a $4 \times 4 \times 1$ ($2 \times 2 \times n$ supercells) or a $2 \times 2 \times 1$ ($4 \times 4 \times n$ supercells) Monkhorst-Pack mesh. The Kohn-Sham wave functions were expanded on a numerical grid with a grid spacing of 0.18 Å. To accelerate convergence, orbital occupations were smeared using a Fermi-Dirac distribution with temperature $k_B T = 0.5$ eV unless otherwise stated. All total energies were extrapolated to 0 K. These parameters were verified to be adequate for obtaining converged work functions and lattice constants.

Charge transfer at the ideal Ag(111)/Au(111) interface was modeled using a 7-layer thick (2×2) Ag slab that was covered with an Au overlayer 1-4 layers thick. 15 Å of vacuum was placed on top of and below each of the studied surface slabs. Periodic boundary conditions were applied in directions parallel to the surface. All configurations were relaxed so that the maximum force on each atom was below 0.05 eV/Å. The two bottom Ag layers were frozen during geometry optimization. To study the effects of surface morphology, we also investigated systems where a $(4 \times 4 \times 7)$ Ag(111) slab was in contact with an Au island. In total, two different Au island sizes with 1-3 atomic layers were considered, see Figure 6 in the main text.

With computational setup described above, the optimized lattice constants of both $(2 \times 2 \times 7)$ Ag(111) and $(2 \times 2 \times 7)$ Au(111) were 4.14 Å, which are slightly higher than the

experimental values 4.09 Å and 4.08 Å.[S12] The calculated work functions 4.42 eV for Ag(111) and 5.14 eV for Au(111), using a smearing temperature of $k_BT = 0.1$ eV, match previous experimental estimates 4.46 ± 0.02 eV[S13] and 5.26 ± 0.04 eV,[S14] respectively.

Interfacial Ag-Au contact areas were estimated from solvent accessible surface areas[S15–S17] (SASAs) using a probe radius of 0.8 Å according to

$$\mathrm{SASA_{interface}} = \frac{\mathrm{SASA_{Ag}} + \mathrm{SASA_{Au}} - \mathrm{SASA_{total}}}{2} \tag{S4}$$

For nonperiodic Au-Ag slabs, the surface coverage of Au, θ, *i.e.* the fraction of Au at the metal-vacuum boundary was directly calculated from SASAs

$$\theta_{\text{no PBC}} = \frac{\mathrm{SASA_{Au}} - \mathrm{SASA_{interface}}}{\mathrm{SASA_{total}} - \mathrm{SASA_{interface}}} \tag{S5}$$

In similar fashion, the surface coverage of Au in nanoislands systems can be evaluated from

$$\theta_{\mathrm{nanoisland}} = 1 - \frac{\frac{2}{9}\mathrm{SASA_{Ag}} - \mathrm{SASA_{interface}}}{\frac{2}{9}\mathrm{SASA_{Ag}} - 2\mathrm{SASA_{interface}} + \mathrm{SASA_{Au}}} \tag{S6}$$

where the latter term is the surface coverage of Ag. In calculating the surface coverage of Ag, we have assumed that the fraction of silver's SASA on the fcc(111) surfaces is directly proportional to the number of Ag atoms on the fcc(111) facets divided by the total number of Ag atoms at the vacuum or periodic boundary interfaces (the term $\frac{2}{9}$).

Due to the two different DFT methods employed, the calculated Fermi levels for nanoparticle and surface systems are not directly comparable. In particular, for surfaces, the calculated value matches the thermodynamic definition of the Fermi level *i.e.* it is the energy of the electronic state with 1/2 occupation; whereas for nanoparticles, the actual quantity calculated is the Fermi *energy*, that is, the energy of the highest occupied molecular orbital. To avoid confusion, we have nonetheless referred to both quantities as Fermi level. This difference in definitions has no bearing on our analysis of charge transfer trends or related

quantities, since all the results are analyzed system specifically and no comparisons between systems are performed.

3 Charge Transfer at Bimetallic Nanoparticles

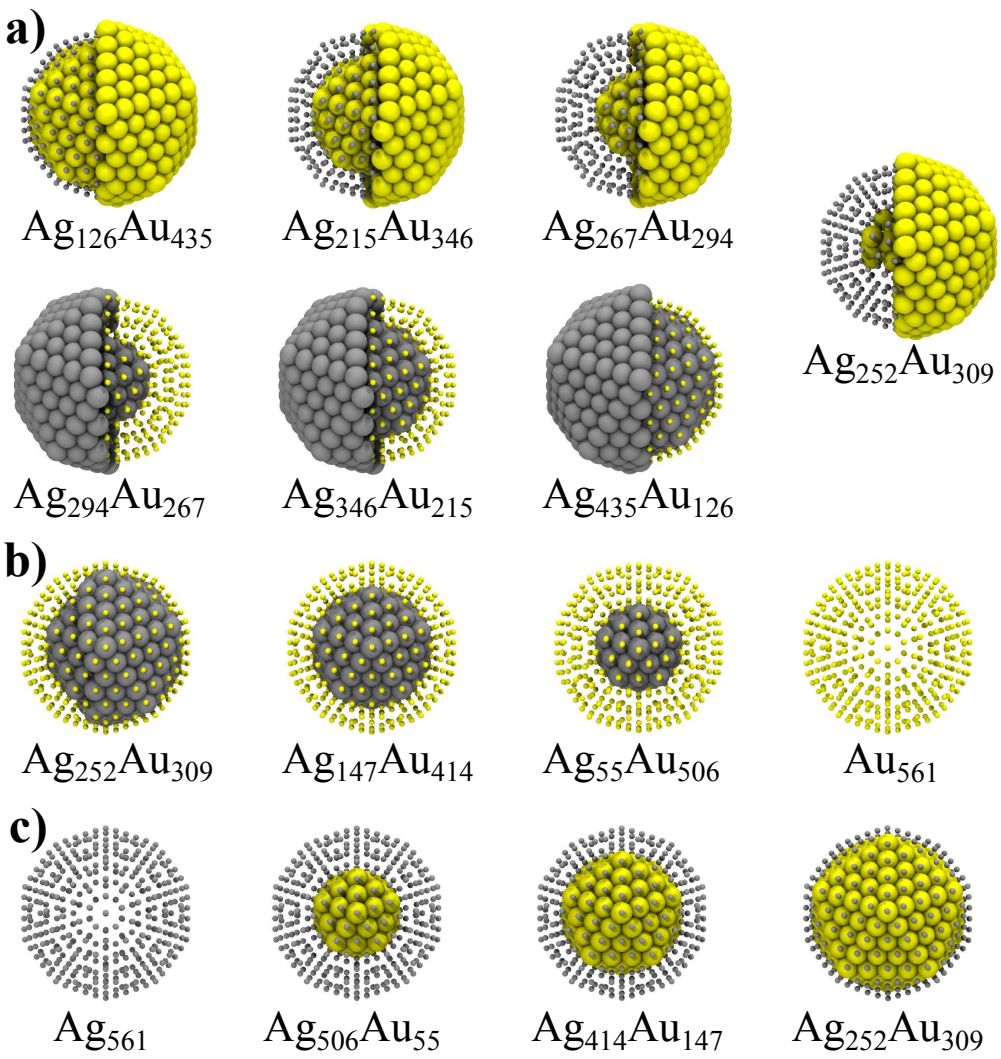

Figure S1. Optimized structures of nanoparticles with 50 (Janus particles, **a**), 0 (**b**), and 100 % (**c**) of Ag in the shell layer. The atomic composition of the nanoparticles is indicated. Nanoparticles with composition $Ag_{252}Au_{309}$ are same as those in Figure 1 of the main text.

Table S1. Net charge transferred (in e) from Ag to Au in bimetallic nanoparticles of different chemical composition. The contact area A (in Å^2) and the average contact distance d (in Å) at the Ag-Au interface used in the capacitance model are also included. The fraction of Au in the outermost layer of the nanoparticle is indicated in the second column.

Nanoparticle	Au fraction in outer shell	Charge transferred	A	d
$Ag_{126}Au_{435}$	0.5	8.45	1176.66	0.252
$Ag_{215}Au_{346}$	0.5	10.51	1087.45	0.264
$Ag_{252}Au_{309}$	0.5	8.49	901.64	0.282
$Ag_{267}Au_{294}$	0.5	9.48	950.87	0.273
$Ag_{294}Au_{267}$	0.5	8.39	948.64	0.271
$Ag_{346}Au_{215}$	0.5	9.97	1064.84	0.266
$Ag_{435}Au_{126}$	0.5	12.58	1125.65	0.286
$Ag_{252}Au_{309}$	0.0	11.66	1773.16	0.245
$Ag_{414}Au_{147}$	0.0	10.42	1081.95	0.233
$Ag_{506}Au_{55}$	0.0	5.85	554.53	0.212
$Ag_{55}Au_{506}$	1.0	4.43	546.80	0.233
$Ag_{147}Au_{414}$	1.0	10.10	1051.69	0.240
$Ag_{252}Au_{309}$	1.0	17.59	1574.79	0.270
$Ag_{252}Au_{309}$	0.75	13.13	1260.59	0.282
$Ag_{252}Au_{309}$	0.25	11.09	1457.24	0.264

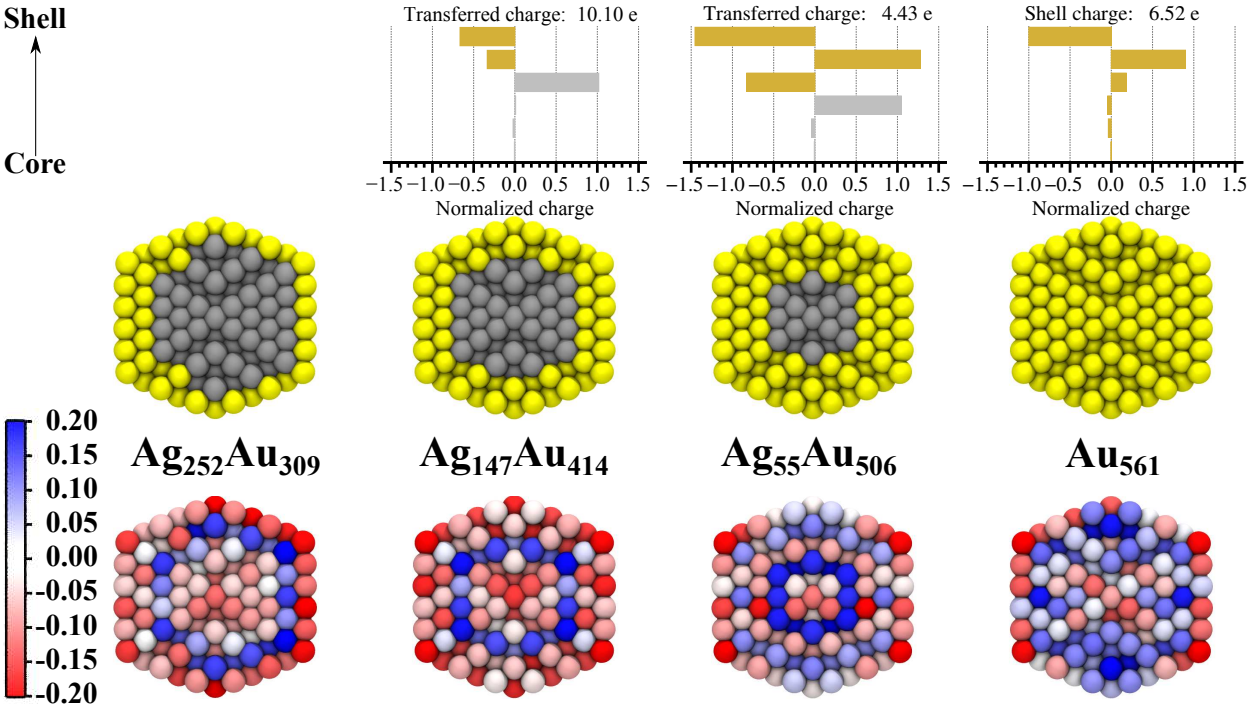

Figure S2. Effect of core size on charge distribution in core-shell nanoparticles. At bottom, cross sections of the nanoparticles demonstrating the inhomogeneous distribution of charge onto individual atoms (bottom), with the actual atomic structure given for reference in the middle panel. At top, layer-by-layer net charge distributions. The charges have been normalized by the total amount of transferred charge from Ag to Au, which is particle dependent. A negative normalized charge indicates an electron excess. No layer-by-layer charge distribution is given for $Ag_{252}Au_{309}$, since one of the layers contains both Ag and Au. The limiting case of a pure Au nanoparticle is included for reference, with charges normalized by the shell charge. Note, only a single atomic plane is visible in the cross sections, whereas all atoms are included in the layer-by-layer averaging.

4 Charge Transfer at Bimetallic Surfaces

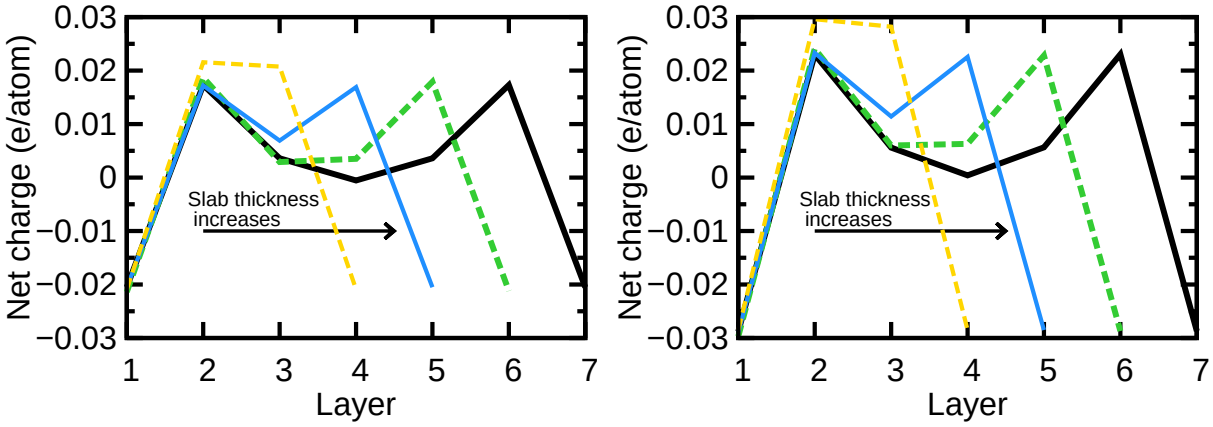

Figure S3. Distribution of net charge in (2×2) Ag(111) (left) and Au(111) (right) as a function of slab thickness. Net charges are given as multiplies of the elementary charge e and are divided by the number of atoms in each atomic layer. Negative values correspond to electron density excess.

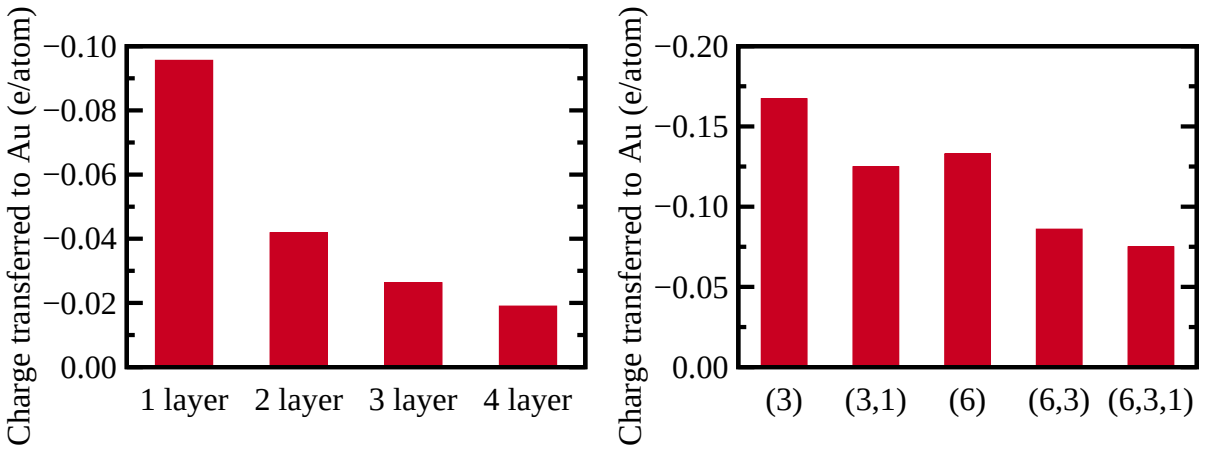

Figure S4. Total charge transferred from Ag to Au in a combined system of seven Ag(111) layers in contact with Au(111) overlayers of different thickness (left) and in systems where $(4 \times 4 \times 7)$ Ag(111) is covered by various Au nanoislands. Charges have been normalized by the total number of Au atoms.

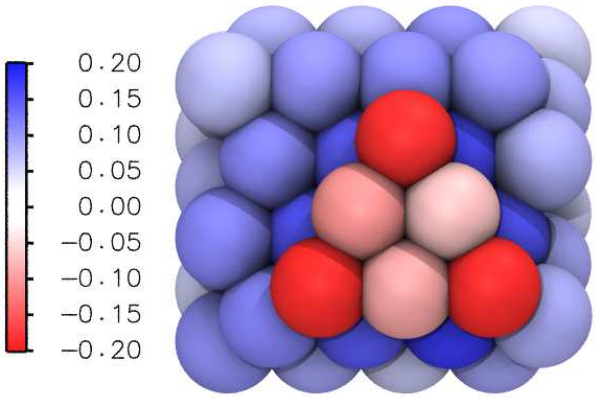

Figure S5. Atomic distribution of charge in a system where a $(4 \times 4 \times 7)$ Ag(111) slab is covered by a (6) Au nanoisland. The net charge of Au is not equally divided onto all atoms since the charge on corner gold atoms is ~ 2 greater than on other Au atoms.

Table S2. The contact area A (in Å^2) and the average contact distance d (in Å) at the Ag-Au interface used in the capacitance model for the indicated bimetallic surface slab and nanoisland systems. The fraction of Au in the outermost layer of the nanoparticle is indicated in the second column.

System Au structure	Au fraction in outer shell	A	d
1 layer	0.50	48.44	2.951
2 layer	0.50	52.94	2.942
3 layer	0.50	52.81	2.938
4 layer	0.50	52.06	2.914
(6) nanoisland	0.39	97.67	2.852
(6, 3) nanoisland	0.42	100.03	2.845
(6, 3, 1) nanoisland	0.48	101.96	2.850
(3) nanoisland	0.26	61.53	2.815
(3, 1) nanoisland	0.30	62.55	2.809

5 Finite Element Simulations of the Electrostatics of a Bimetallic Janus Particle

The icosahedral Janus particle with composition $Ag_{294}Au_{267}$ was approximated as a sphere with an inner radius of 5.03 Å and an outer radius of 12.58 Å, as shown in Figure S6. The sharp corners were rounded with a radius of 0.1 Å.

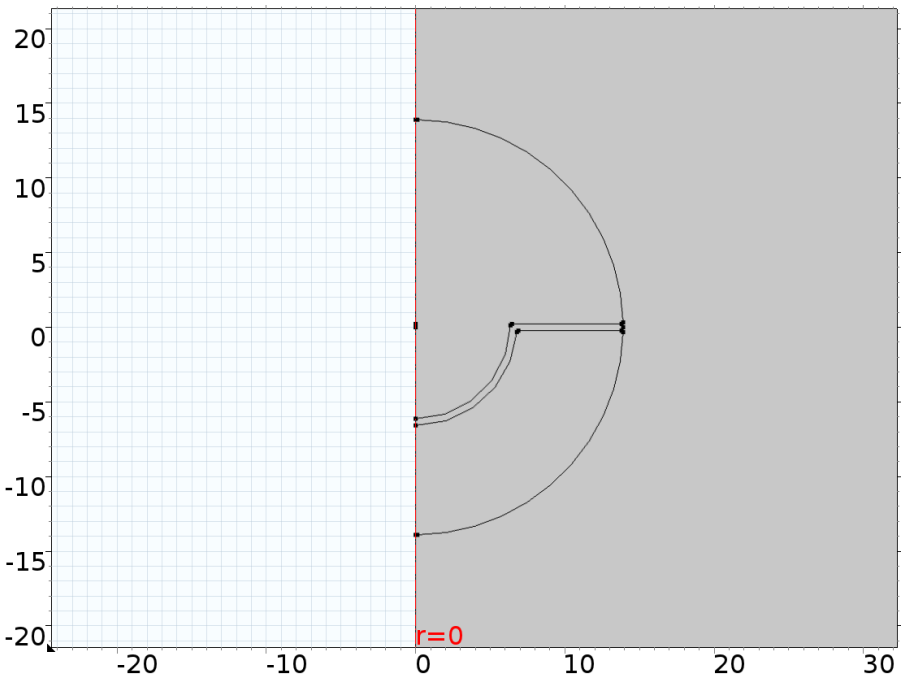

Figure S6. COMSOL model system for Janus particle with composition $Ag_{294}Au_{267}$.

The electrostatics of the system were described by the Poisson equation:

$$\mathbf{E} = -\nabla V \tag{S7}$$

where V is the electric potential, and $\mathbf{E}$ is the electric field. Charge conservation is obeyed in all domains:

$$\nabla \cdot (\boldsymbol{\varepsilon_0 \varepsilon_r} \mathbf{E}) = \rho_v \tag{S8}$$

where $\boldsymbol{\varepsilon_0}$ and $\boldsymbol{\varepsilon_r}$ are permittivity of vacuum and the relative permittivity, and ρ_v is the

space charge density.

The model was solved in 2D axial symmetry (r = 0 as the axis of symmetry). The electric potential is set to 0.43 V on the silver boundaries, and to –0.43 V on the gold boundaries, and the boundary of the surrounding vacuum (10 000 Å away) is set to have a zero surface charge density. The mesh density was increased until the results did not significantly change. The width of the gap between Ag and Au was adjusted so that the amount of charge transfer corresponded to the value (8.4 e) obtained with DFT calculations.

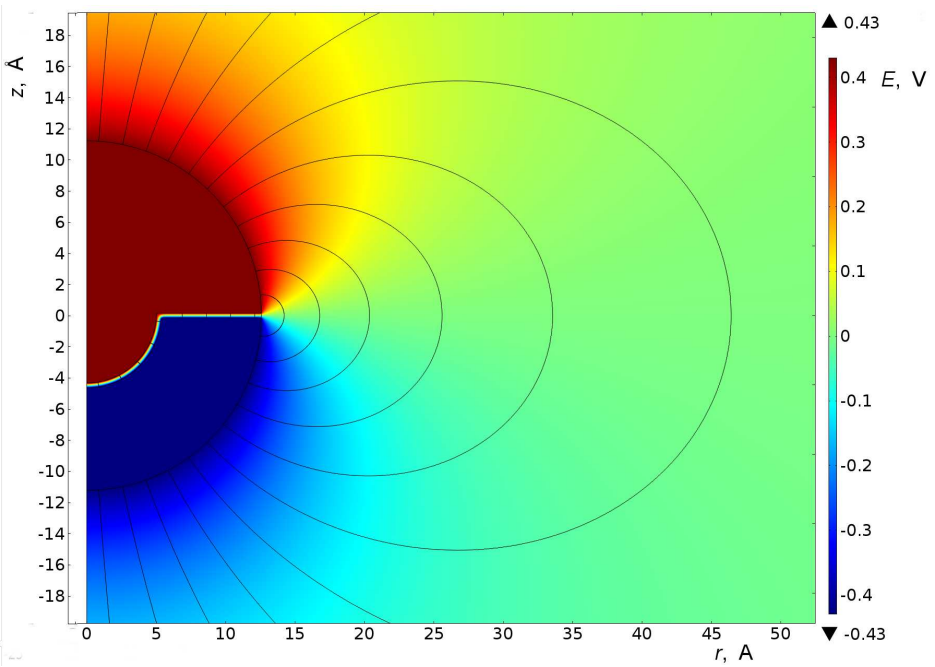

Figure S7. The potential distribution of an $Ag_{294}Au_{267}$ Janus particle approximated as a sphere, shown in 2D axial symmetry. The silver part is charged positively, at a potential of 0.43 V while gold is at -0.43 V with a negative surface charge.

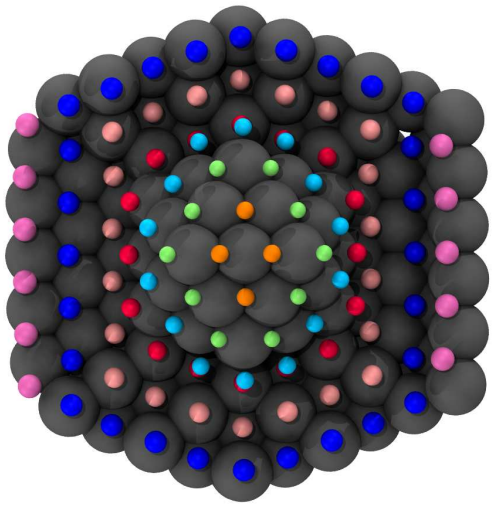

Figure S8. Schematic illustration showing how the arc length in Figure 6 is defined for DFT simulations. Silver atoms at the contact interface are visualized as large, gray spheres, while the smaller spheres are gold atoms. The gold atoms are color coded according to which layer they belong to as counted outwards from the center of the nanoparticle. The arc length is defined as the cumulative sum over the average distance between different gold layers.

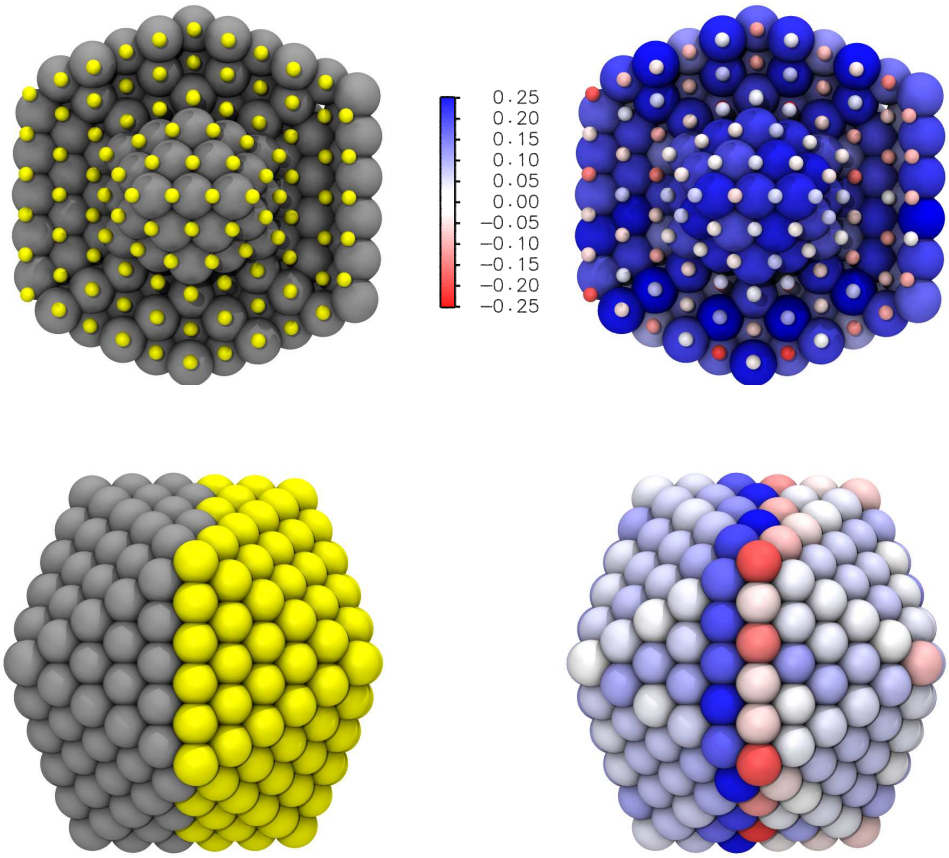

Figure S9. Atomic charge distribution at the interface between gold and silver for the Janus particle with composition $Ag_{294}Au_{267}$ visualized along the contact surface (top) and perpendicular to it (bottom). For both view angles, the left figure shows the relative positioning of Au (yellow) and Ag (gray) atoms, whereas in the right figure atoms are colored according to their net charge. The charge is inhomogeneously distributed within the layers that were employed for defining the arc length in Figure S8.

References

(S1) Girault, H. *Analytical and Physical Electrochemistry*; EFPL Press, 2004.

(S2) Perdew, J. P.; Burke, K.; Ernzerhof, M. Generalized Gradient Approximation Made Simple. *Phys. Rev. Lett.* **1996**, *77*, 3865–3868.

(S3) VandeVondele, J.; Krack, M.; Mohamed, F.; Parrinello, M.; Chassaing, T.; Hutter, J. Quickstep: Fast and Accurate Density Functional Calculations Using a Mixed Gaussian and Plane Waves Approach. *Comput. Phys. Commun.* **2005**, *167*, 103–128.

(S4) Hutter, J.; Iannuzzi, M.; Schiffmann, F.; VandeVondele, J. CP2K: Atomistic Simulations of Condensed Matter Systems. *Wiley Interdiscip. Rev.: Comput. Mol. Sci.* **2014**, *4*, 15–25.

(S5) VandeVondele, J.; Hutter, J. Gaussian Basis Sets for Accurate Calculations on Molecular Systems in Gas and Condensed Phases. *J. Chem. Phys.* **2007**, *127*, 114105–9.

(S6) Goedecker, S.; Teter, M.; Hutter, J. Separable Dual-Space Gaussian Pseudopotentials. *Phys. Rev. B* **1996**, *54*, 1703–1710.

(S7) Hartwigsen, C.; Goedecker, S.; Hutter, J. Relativistic Separable Dual-Space Gaussian Pseudopotentials from H to Rn. *Phys. Rev. B* **1998**, *58*, 3641–3662.

(S8) Krack, M. Pseudopotentials for H to Kr Optimized for Gradient-Corrected Exchange-Correlation Functionals. *Theor. Chem. Acc.* **2005**, *114*, 145–152.

(S9) Martyna, G. J.; Tuckerman, M. E. A Reciprocal Space Based Method for Treating Long Range Interactions in Ab Initio and Force-Field-Based Calculations in Clusters. *J. Chem. Phys.* **1999**, *110*, 2810–2821.

(S10) Henkelman, G.; Arnaldsson, A.; Jónsson, H. A Fast and Robust Algorithm for Bader Decomposition of Charge Density. *Comput. Mater. Sci.* **2006**, *36*, 354 – 360.

(S11) Enkovaara, J.; Rostgaard, C.; Mortensen, J. J.; Chen, J.; Dułak, M.; Ferrighi, L.; Gavnholt, J.; Glinsvad, C.; Haikola, V.; Hansen, H. A.; Kristoffersen, H. H.; Kuisma, M.; Larsen, A. H.; Lehtovaara, L.; Ljungberg, M.; Lopez-Acevedo, O.; Moses, P. G.; Ojanen, J.; Olsen, T.; Petzold, V.; Romero, N. A.; Stausholm-Møller, J.; Strange, M.; Tritsaris, G. A.; Vanin, M.; Walter, M.; Hammer, B.; Häkkinen, H.; Madsen, G. K. H.; Nieminen, R. M.; Nørskov, J. K.; Puska, M.; Rantala, T. T.; Schiøtz, J.; Thygesen, K. S.; Jacobsen, K. W. Electronic Structure Calculations with GPAW: A Real-Space Implementation of the Projector Augmented-Wave Method. *J. Phys. Condens. Matter* **2010**, *22*, 253202.

(S12) *CRC Handbook of Chemistry and Physics*, 70th ed.; CRC Press: Boca Raton, FL, USA, 1990.

(S13) Chelvayohan, M.; Mee, C. H. B. Work Function Measurements on (110), (100) and (111) Surfaces of Silver. *J. Phys. C: Solid State Phys.* **1982**, *15*, 2305.

(S14) Hansson, G. V.; Flodström, S. A. Photoemission Study of the Bulk and Surface Electronic Structure of Single Crystals of Gold. *Phys. Rev. B* **1978**, *18*, 1572–1585.

(S15) Lee, B.; Richards, F. The Interpretation of Protein Structures: Estimation of Static Accessibility. *J. Mol. Biol.* **1971**, *55*, 379 – IN4.

(S16) Varshney, A.; Brooks, F. P.; Wright, W. V. Linearly Scalable Computation of Smooth Molecular Surfaces. *IEEE Comput. Graph. Appl. Mag.* **1994**, *14*, 19–25.

(S17) Humphrey, W.; Dalke, A.; Schulten, K. VMD – Visual Molecular Dynamics. *J. Mol. Graphics* **1996**, *14*, 33–38.